



ARTICLE

An Efficient Local Radial Basis Function Method for Image Segmentation Based on the Chan–Vese Model

Shupeng Qiu, Chujin Lin and Wei Zhao*

School of Mathematics and Statistics, Guangdong University of Technology, Guangzhou, 510520, China

*Corresponding Author: Wei Zhao. Email: wzhao@gdut.edu.cn

Received: 02 May 2023 Accepted: 28 July 2023 Published: 30 December 2023

ABSTRACT

In this paper, we consider the Chan–Vese (C–V) model for image segmentation and obtain its numerical solution accurately and efficiently. For this purpose, we present a local radial basis function method based on a Gaussian kernel (GA-LRBF) for spatial discretization. Compared to the standard radial basis function method, this approach consumes less CPU time and maintains good stability because it uses only a small subset of points in the whole computational domain. Additionally, since the Gaussian function has the property of dimensional separation, the GA-LRBF method is suitable for dealing with isotropic images. Finally, a numerical scheme that couples GA-LRBF with the fourth-order Runge–Kutta method is applied to the C–V model, and a comparison of some numerical results demonstrates that this scheme achieves much more reliable image segmentation.

KEYWORDS

Image segmentation; Chan–Vese model; local radial basis function method; Gaussian kernel; Runge–Kutta method

1 Introduction

Image segmentation is a challenging and complicated task in the field of image processing and has a wide range of applications in computer vision, such as medical image analysis, autonomous driving, remote sensing, security and protection monitoring [1–3]. The major task of image segmentation is to divide a prescribed image into several nonoverlapping and disjoint regions according to characteristics such as color, gray level (intensity) and geometric shape. With the increasing demand for segmentation techniques, many methods have been proposed, including threshold-based methods, region-based methods, edge-based methods, PDE-based methods and emerging methods based on deep neural networks. Among these representative classes of methods, the latter two correspond to mainstream algorithms. Nevertheless, although deep learning methods such as fully convolutional networks perform well in terms of accuracy [4], they are not fully interpretable and require considerable time for neural network training. An image itself can be regarded as a discrete two-dimensional matrix, which can be modeled using continuous mathematical models based on partial differential equations (PDEs). Over the decades, PDE-based models have shown excellent applicability and efficiency due to their high mathematical significance. Among PDE-based models, active contour models are some of the most popular, including the parametric active contour model and the level set method. A parametric



active contour model (Snakes) was first proposed by Kass et al. [5]; however, in this model, the curves cannot enter deep areas of the image, and the initial curves must already be close to the edges of the image contours. To handle this limitation, the level set method was presented for flexibly handling topological changes in images [6–9]. In this method, a contour curve is embedded into a higher-dimensional function, representing that the level sets of different topological structures in the evolutionary process all correspond to the same level. Therefore, such a level set function can automatically control topological changes. The Chan–Vese (C-V) model is a typical level set model using a variational principle [10], as an improved variant of the Mumford–Shah (M-S) model [11], in which the complex functional is simplified by assuming that the gray levels within homogeneous regions of an image are constant. Many works have proven that the C-V model can effectively improve the topological adaptation ability in curve evolution; therefore, it is a powerful tool for image segmentation and has attracted increasing attention from researchers [12–14].

Once the desired model has been derived, numerical simulation plays an important role in understanding the dynamic evolutionary process of active contours. At present, the finite differential method (FDM) has been widely applied to numerically solve the PDEs originating from the level set method in most cases; this method achieves reasonably satisfactory accuracy [11] but is computationally expensive. In addition, various traditional techniques and algorithms have been used to optimize the accuracy and results of image segmentation. Nonetheless, limited by the efficiency and data processing ability of these algorithms, many challenges still arise in practical applications. In recent years, the radial basis function (RBF) method has attracted much attention because of its simple format and high accuracy [15–19], and it has gradually developed into a significant numerical method in the scientific computing domain [20–23]. However, for large-scale problems such as image processing, the RBF method incurs excessive computational costs due to the generation of a dense matrix [23–26], and the large condition number of this matrix can also cause calculation instability [27,28]. To conquer this shortcoming, local RBF (LRBF) methods based on positive and conditionally positive global kernels have been developed, such as [29], which consider only the contributions from several neighboring points in the near field while ignoring the influence of distant points. The corresponding sparse interpolation matrix apparently reduces the condition number of the matrix, saves storage space and enhances computational efficiency. Other newly developed local methods, such as [30–32], can also be applied to achieve these benefits.

In this paper, based on a Gaussian (GA) kernel, a new LRBF scheme is developed for solving the C-V model accurately and efficiently. Specifically, since a high-dimensional exponential function can be separated along each dimension, the GA-RBF interpolation can be expressed in the form of a tensor product of multiple one-dimensional interpolations. This approach eliminates the isotropic property of radial basis functions; thus, it is suitable for treating inhomogeneous image problems, and afterward, a local scheme is obtained accordingly.

The remainder of this paper is organized as follows: Section 2 provides a brief review of the C-V segmentation model. Section 3 gives more details of the proposed LRBF method based on a Gaussian kernel and presents a fully discrete system obtained by combining the proposed method with the fourth-order Runge–Kutta method. Several numerical experiments are presented in Section 4 to verify the performance of the proposed method, including its accuracy, efficiency and stability. Finally, some conclusions and plans for further research are reported in Section 5.

2 Mathematical Model

In this section, we give a brief review of the C-V model, which is an active contour model for two-phase segmentation based on the Mumford–Shah model. Let Ω be a bounded domain of \mathbb{R}^2 , with the boundary $\partial\Omega$. Let I be a given image, and let $C(s)$ be a parameterized closed curve. Classical snakes and active contour models are designed to minimize the following energy functional:

$$E(c_1, c_2, C) = \mu L(C) + \lambda_1 \int_{in(C)} |I - c_1|^2 dx dy + \lambda_2 \int_{out(C)} |I - c_2|^2 dx dy, \tag{1}$$

where $L(C)$ is the length of C ; $out(C)$ and $in(C)$ represent the regions outside and inside of C , respectively; c_1 and c_2 are two constants that denote the average intensities inside and outside of C , respectively; and μ, λ_1 , and λ_2 are fixed nonnegative parameters. The first term controls the smoothness of the contour, while the latter two terms attract the contour toward objects in the image.

In problems of curve evolution, the level set method and, in particular, the ‘motion by mean curvature’ approach of Osher et al. [6] have been used extensively. The curve C is implicitly represented via a Lipschitz function ϕ , i.e., $C = \{(x, y) | \phi(x, y) = 0\}$, and the evolution of the curve is given by the zero-level curve at time t of the function $\phi(x, y, t)$, as shown in Fig. 1.

$$\begin{cases} \phi(x, y) = 0, & (x, y) \in C, \\ \phi(x, y) > 0, & (x, y) \in in(C), \\ \phi(x, y) < 0, & (x, y) \in out(C). \end{cases} \tag{2}$$

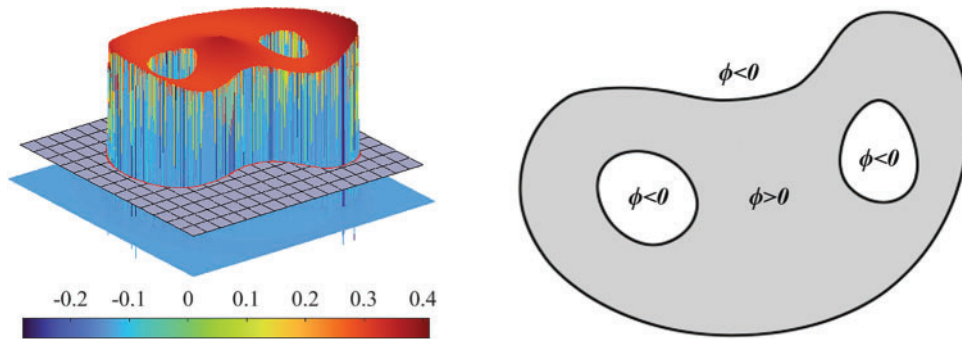


Figure 1: The level set function graph (left) and the zero-level curve graph (right)

With the introduction of the Heaviside function H and the Dirac measure δ_0 , defined, respectively, as

$$H(\phi) = \begin{cases} 1, & (x, y) \geq 0, \\ 0, & (x, y) < 0, \end{cases} \quad \text{and} \quad \delta(\phi) = \frac{dH}{d\phi}, \tag{3}$$

the terms in the energy functional have the following forms:

$$L\{\phi = 0\} = \int_{\Omega} |\nabla H(\phi(x, y))| dx dy = \int_{\Omega} \delta_0(\phi(x, y)) |\nabla \phi(x, y)| dx dy \tag{4}$$

$$\int_{\phi > 0} |I(x, y) - c_1|^2 dx dy = \int_{\Omega} |I(x, y) - c_1|^2 H(\phi(x, y)) dx dy, \tag{5}$$

and

$$\int_{\phi < 0} |I(x, y) - c_1|^2 dx dy = \int_{\Omega} |I(x, y) - c_1|^2 (1 - H(\phi(x, y))) dx dy. \quad (6)$$

Thus, the energy $E(c_1, c_2, \phi)$ can be written as

$$\begin{aligned} E(c_1, c_2, \phi) = & \mu \int_{\Omega} \delta(\phi(x, y)) |\nabla \phi(x, y)| dx dy + \lambda_1 \int_{\Omega} |I(x, y) - c_1|^2 H(\phi(x, y)) dx dy \\ & + \lambda_2 \int_{\Omega} |I(x, y) - c_1|^2 (1 - H(\phi(x, y))) dx dy. \end{aligned} \quad (7)$$

By keeping ϕ fixed and minimizing the energy $E(c_1, c_2, \phi)$ with respect to the constants c_1 and c_2 , it is easy to express these constants as functions of ϕ , as follows:

$$c_1(\phi) = \frac{\int_{\Omega} I(x, y) H(\phi(x, y)) dx dy}{\int_{\Omega} H(\phi(x, y)) dx dy} \quad \text{and} \quad c_2(\phi) = \frac{\int_{\Omega} I(x, y) (1 - H(\phi(x, y))) dx dy}{\int_{\Omega} (1 - H(\phi(x, y))) dx dy}. \quad (8)$$

For the corresponding “degenerate” cases, there are no constraints on the values of c_1 and c_2 . Then, c_1 and c_2 are in fact given by [10]

$$\begin{cases} c_1(\phi) = \text{average}(I) \text{ in } \{\phi \geq 0\}, \\ c_2(\phi) = \text{average}(I) \text{ in } \{\phi < 0\}. \end{cases} \quad (9)$$

By the calculus of variations, the Gateaux derivative of the functional E can be written as

$$\frac{\partial E}{\partial \phi} = -\delta(\phi) \left[\mu \nabla \cdot \left(\frac{\nabla \phi}{|\nabla \phi|} \right) - \lambda_1 (I - c_1)^2 + \lambda_2 (I - c_2)^2 \right].$$

Therefore, the function ϕ that minimizes this functional satisfies the Euler–Lagrange equation $\frac{\partial E}{\partial \phi} = 0$. The steepest descent process for minimization of the functional E corresponds to the following gradient flow:

$$\frac{\partial \phi}{\partial t} = \delta(\phi) \left[\mu \nabla \cdot \left(\frac{\nabla \phi}{|\nabla \phi|} \right) - \lambda_1 (I - c_1)^2 + \lambda_2 (I - c_2)^2 \right]. \quad (10)$$

3 Numerical Method

3.1 The Global Radial Basis Function (GRBF) Method

In this section, we introduce the RBF method for the interpolation of scattered data. For a set of N distinct centers $\{\mathbf{x}_1, \mathbf{x}_2, \dots, \mathbf{x}_N\}$ in $\Omega \subset \mathbb{R}^n$, an approximation $\hat{f}(\mathbf{x})$ of a function $f(\mathbf{x})$ can be written in the form of a linear combination of radial basis functions (RBFs) as follows:

$$f(\mathbf{x}) \approx \hat{f}(\mathbf{x}) = \sum_{j=1}^N \alpha_j \Phi(\|\mathbf{x} - \mathbf{x}_j\|), \quad \mathbf{x} \in \Omega, \quad (11)$$

where $\Phi(\cdot)$ represents an RBF. Commonly used types of RBFs are listed in Table 1, in which $r = \|\cdot\|$ is the Euclidean distance and $c > 0$ is the shape parameter. The coefficients α_j are obtained from the interpolation conditions at \mathbf{x}_i :

$$f(\mathbf{x}_i) = \hat{f}(\mathbf{x}_i), \quad i = 1, 2, \dots, N. \quad (12)$$

Table 1: Three common RBFs

Type of basis kernel	$\Phi(r)$
Gaussian (GA)	$\exp(-(cr)^2)$
Multiquadric (MQ)	$\sqrt{1+(cr)^2}$
Inverse multiquadric (IMQ)	$\frac{1}{\sqrt{1+(cr)^2}}$

Therefore, the following linear system of algebraic equations must be solved:

$$\mathbf{A}\boldsymbol{\alpha} = \mathbf{f}, \tag{13}$$

where $\mathbf{A} = [\Phi(\|\mathbf{x}_i - \mathbf{x}_j\|)]$, $i, j = 1, 2, \dots, N$, $\boldsymbol{\alpha} = [\alpha_1, \alpha_2, \dots, \alpha_N]^T$, and $\mathbf{f} = [f(\mathbf{x}_1), f(\mathbf{x}_2), \dots, f(\mathbf{x}_N)]^T$. After solving this system, the approximation of $f(\mathbf{x})$ and its k -th order derivative can be obtained at any point in Ω as

$$f^{(k)}(\mathbf{x}) \approx \hat{f}^{(k)}(\mathbf{x}) = \sum_{j=1}^N \Psi_j^{(k)}(\mathbf{x})f(\mathbf{x}_j), \quad k = 0, 1, 2, \dots \tag{14}$$

Because it always generates a dense interpolation matrix \mathbf{A} , the standard RBF method is a global method that consumes more CPU time for larger-scale problems and can lead to unstable results because of ill-conditioned numbers. To handle these difficulties, we introduce the concept of local interpolation into the GRBF method. That is, for each evaluation point, we consider contributions only from its neighbors in the near field and ignore the effects from the far field. Because a sparse interpolation matrix is generated, this approach consumes less computing time.

3.2 Local Radial Basis Function Method Based on a GA Kernel (GA-LRBF)

For simplicity, we describe the method in two dimensions. $\hat{u}(x, y)$ can be represented as an expansion of Gaussian radial basis functions:

$$\hat{u}(x, y) = \sum_{j=1}^{N_x} \sum_{k=1}^{N_y} \alpha_{jk} \Phi_{jk}(x, y), \tag{15}$$

where $\Phi_{jk}(x, y) = \exp(-c^2((x - x_j)^2 + (y - y_k)^2))$. Since exponential functions have the property of separation, Eq. (15) can be written as

$$\hat{u}(x, y) = \sum_{j=1}^{N_x} \sum_{k=1}^{N_y} \alpha_{jk} \Phi_j(x) \cdot \Phi_k(y) := [\Phi_j(x) \otimes \Phi_k(y)]\boldsymbol{\alpha}. \tag{16}$$

From the interpolation conditions on the data points (x_m, y_n) ($m = 1, 2, \dots, N_x$; $n = 1, 2, \dots, N_y$), we obtain the coefficient vector, and the approximation can be written as

$$\begin{aligned} \hat{u}(x, y) &= [\Phi_j(x)\Phi_j^{-1}(x_m)] \otimes [\Phi_k(y)\Phi_k^{-1}(y_n)]\mathbf{u} \\ &:= \sum_{j=1}^{N_x} \sum_{k=1}^{N_y} \Psi_j(x)\Psi_k(y)u(x_j, y_k), \end{aligned} \tag{17}$$

where $\Psi_j(x)$ and $\Psi_k(y)$ satisfy the interpolation conditions, i.e.,

$$\Psi_j(x_i) = \begin{cases} 1, & i = j, \\ 0, & i \neq j, \end{cases} \quad \text{and} \quad \Psi_k(y_s) = \begin{cases} 1, & k = s, \\ 0, & k \neq s. \end{cases} \quad (18)$$

To improve the stability of RBF interpolation, a localized approach was recently developed. The distinctive feature of this method is that only a few neighboring points are needed. Because it generates a sparse interpolation matrix, it consumes less computing time. Specifically, for points (x_s, y_l) ($s = 1, 2, \dots, N_x; l = 1, 2, \dots, N_y$), the local interpolation has the following form:

$$\hat{u}(x_s, y_l) = \sum_{j=1}^{M_s} \sum_{k=1}^{M_l} \Psi_j(x_s) \Psi_k(y_l) u(x_j, y_k), \quad (19)$$

where M_s and M_l are the numbers of closest points for x_s and y_l , respectively. Since $M_s \ll N_x$ and $M_l \ll N_y$, all local $M_s \times M_l$ matrices can be extended to an $N_x \times N_y$ global matrix by filling in zeros, and the obtained matrix is sparse. In particular, if $M_s = M_l = 3$, the LRBF method becomes an FDM-type scheme, as shown in Fig. 2, while if $M_s = N_x$ and $M_l = N_y$, the LRBF method degenerates to the standard GRBF method. Compared with the GRBF method, this scheme consumes less CPU time because it yields a sparse interpolation matrix, and it maintains good stability because it uses only a small subset of points in the whole computational domain. Additionally, since the Gaussian kernel adopted as the RBF has the natural property of dimensional separation, the GA-LRBF method requires the storage of only a one-dimensional interpolation matrix and thus occupies less memory for numerical computation. Consequently, this method is suitable for dealing with isotropic images and efficient at manipulating massive-scale image information. However, different from [31,32], our proposed GA-LRBF method is essentially similar to the GRBF method but formally similar to the FDM; hence, the spatial derivative magnitude of ϕ is highly unlikely to be zero, meaning that this scheme can be freely applied.

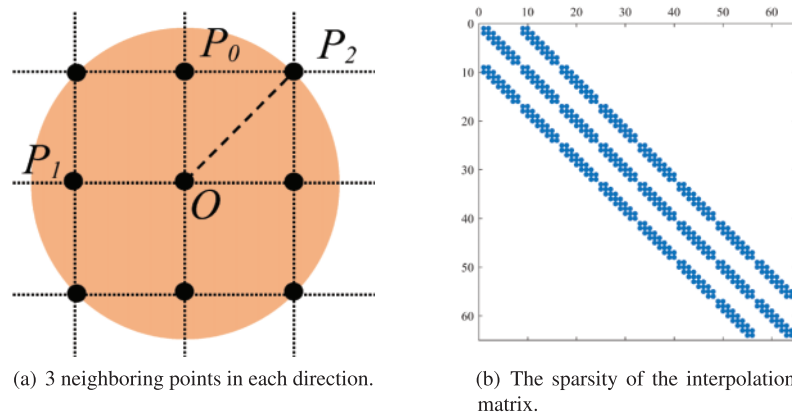


Figure 2: The GA-LRBF scheme with 3 neighboring points in each direction has a form similar to that of the FDM scheme. (a) 3 neighboring points in each direction. (b) The sparsity of the corresponding interpolation matrix

To implement the GA-LRBF method for solving the C-V model, it is necessary to compute the differential operator

$$\nabla \cdot \left(\frac{\nabla \phi}{|\nabla \phi|} \right) = \frac{\phi_{xx}\phi_y^2 - 2\phi_x\phi_y\phi_{xy} + \phi_{yy}\phi_x^2}{(\phi_x^2 + \phi_y^2)^{3/2}}, \quad (20)$$

which involves spatial derivative terms expressed as

$$\phi_x(x_s, y_l) \approx \sum_{j=1}^{M_s} \frac{d\Psi_j(x_s)}{dx} \sum_{k=1}^{M_l} \Psi_k(y_l) \phi(x_j, y_k), \quad (21)$$

$$\phi_y(x_s, y_l) \approx \sum_{j=1}^{M_s} \Psi_j(x_s) \sum_{k=1}^{M_l} \frac{d\Psi_k(y_l)}{dy} \phi(x_j, y_k), \quad (22)$$

$$\phi_{xy}(x_s, y_l) \approx \sum_{j=1}^{M_s} \frac{d\Psi_j(x_s)}{dx} \sum_{k=1}^{M_l} \frac{d\Psi_k(y_l)}{dy} \phi(x_j, y_k), \quad (23)$$

$$\phi_{xx}(x_s, y_l) \approx \sum_{j=1}^{M_s} \frac{d^2\Psi_j(x_s)}{dx^2} \sum_{k=1}^{M_l} \Psi_k(y_l) \phi(x_j, y_k), \quad (24)$$

and

$$\phi_{yy}(x_s, y_l) \approx \sum_{j=1}^{M_s} \Psi_j(x_s) \sum_{k=1}^{M_l} \frac{d^2\Psi_k(y_l)}{dy^2} \phi(x_j, y_k). \quad (25)$$

After the GA-LRBF method is applied to the C-V model, it can be expressed as a time-dependent semidiscrete nonlinear system

$$\sum_{j=1}^{M_s} \sum_{k=1}^{M_l} \frac{\partial \Psi_j(x_s) \Psi_k(y_l)}{\partial t} \phi(x_j, y_k) = \delta \left(\sum_{j=1}^{M_s} \sum_{k=1}^{M_l} \Psi_j(x_s) \Psi_k(y_l) \phi(x_j, y_k) \right) [\mu \operatorname{div} - \lambda_1 (I - c_1)^2 + \lambda_2 (I - c_2)^2], \quad (26)$$

$$s = 1, 2, \dots, N_x, l = 1, 2, \dots, N_y,$$

where $N_x \times N_y$ is the size of the given image,

$$\operatorname{div} = \nabla \cdot \left(\frac{\nabla \phi}{|\nabla \phi|} \right) (x_s, y_l) = \frac{\phi_{xx}(x_s, y_l)\phi_y^2(x_s, y_l) - 2\phi_x(x_s, y_l)\phi_y(x_s, y_l)\phi_{xy}(x_s, y_l) + \phi_{yy}(x_s, y_l)\phi_x^2(x_s, y_l)}{(\phi_x^2(x_s, y_l) + \phi_y^2(x_s, y_l))^{3/2}}, \quad (27)$$

$$c_1 = \frac{\int_{\Omega} I(x, y) H \left(\sum_{j=1}^{M_s} \sum_{k=1}^{M_l} \Psi_j(x_s) \Psi_k(y_l) \phi(x_j, y_k) \right) dx dy}{\int_{\Omega} H \left(\sum_{j=1}^{M_s} \sum_{k=1}^{M_l} \Psi_j(x_s) \Psi_k(y_l) \phi(x_j, y_k) \right) dx dy}, \quad (28)$$

and

$$c_2 = \frac{\int_{\Omega} I(x, y) (1 - H \left(\sum_{j=1}^{M_s} \sum_{k=1}^{M_l} \Psi_j(x_s) \Psi_k(y_l) \phi(x_j, y_k) \right)) dx dy}{\int_{\Omega} (1 - H \left(\sum_{j=1}^{M_s} \sum_{k=1}^{M_l} \Psi_j(x_s) \Psi_k(y_l) \phi(x_j, y_k) \right)) dx dy}. \quad (29)$$

In this section, we consider the fourth-order Runge–Kutta scheme (RK4) for the C-V model. Letting $t_n = n\Delta t$ ($n = 0, 1, \dots, N$) be uniform points in the time interval $[0, T]$ with a time step of $\Delta t = T/N$, we have

$$\begin{cases} \phi_{n+1} = \phi_n + \Delta t/6(K_1 + 2K_2 + 2K_3 + K_4), \\ K_1 = \mathcal{R}(\phi_n, t_n), \\ K_2 = \mathcal{R}(\phi_n + \Delta t/2K_1, t_n + \Delta t/2), \\ K_3 = \mathcal{R}(\phi_n + \Delta t/2K_2, t_n + \Delta t/2), \\ K_4 = \mathcal{R}(\phi_n + \Delta tK_3, t_n + \Delta t), \end{cases} \quad (30)$$

where $\mathcal{R}(\cdot)$ represents the right-hand side of the semidiscrete system.

4 Numerical Experiments

In this section, we report the numerical results obtained from the implementation of the proposed methods in [Section 3](#). For this purpose, we present the following remarks:

- In this paper, all cases are calculated using a time step of $\Delta t = 0.1$ and a GA kernel with a shape parameter value of $c = 1$. How to choose the optimal shape parameter when using the meshless collocation method with the RBF approach is an open problem [27,28]. Given that this is not the focus of our research, we have performed a simple numerical test using the GA-LRBF and GRBF methods with different shape parameter values. The numerical results indicate that the accuracy and efficiency of segmentation using the GA-LRBF method are relatively insensitive to the shape parameter value, but the same is not true for the GRBF method. Therefore, for better comparison in the numerical experiments, an appropriate shape parameter of $c = 1$ is consistently selected.
- In practice, we use the regularized Heaviside function $H_\varepsilon(\phi)$ in [Eq. \(8\)](#), defined as

$$H_\varepsilon(\phi) = \frac{1}{2} \left(1 + \frac{2}{\pi} \arctan \left(\frac{\phi}{\varepsilon} \right) \right), \quad (31)$$

and the corresponding regularized Dirac function $\delta_\varepsilon(\phi)$ in [Eq. \(10\)](#) is given by

$$\delta_\varepsilon(\phi) = \frac{1}{\pi} \frac{\varepsilon}{\varepsilon^2 + \phi^2}. \quad (32)$$

The parameter $\varepsilon = 1$ is selected in the following numerical experiments:

- To verify the influence of the initial contour on the subsequent evolution, we consider two types of initial level set functions. One is a circle contour, which is defined as $\phi_0 = r - \sqrt{(x - c_i)^2 + (y - c_j)^2}$, where c_i and c_j denote the half height and width, respectively, of the image and $r = 1/3c_i$. The other is a constant contour, which is defined as $\phi_0 = 2$ for the entire domain.
- To judge the effectiveness of image segmentation, we consider two classical evaluation indices defined as [33,34]

$$\text{DICE} = \frac{2(A \cap B)}{|A| + |B|} \times 100\%, \quad \text{and} \quad \text{VOE} = \frac{2|A - B|}{|A| + |B|} \times 100\%, \quad (33)$$

where ‘‘DICE’’ measures the spatial overlap between two target regions A and B and ‘‘VOE’’ describes the error ratio of segmentation. For successful image segmentation, the values of ‘‘DICE’’ and ‘‘VOE’’ should tend toward 1 and 0, respectively.

Example 4.1. *The first term of the C-V model, $\mu \nabla \cdot (\nabla \phi / |\nabla \phi|)$, describes the smoothness of the level set function. To test its influence on evolution, we solve the C-V model with various values of the parameter μ by using the GA-LRBF method combined with RK4. The initial contour is taken to be a circle.*

Fig. 3 displays the segmentation results for a 256×256 pixel image based on the C-V model with $\mu = 100, 10, 1, 0.1$ and 0 . It can be observed that smaller parameter values lead to better results; in particular, when μ is zero, there is almost no influence on evolution. The results are listed for comparison in Table 2. Moreover, during iteration, the divergence term imposes a heavy calculation burden. The same analysis is performed in the Appendix using the GRBF method, and we come to a similar conclusion. Consequently, to balance efficiency and accuracy, the parameter μ is taken to be 0 in the following numerical examples.

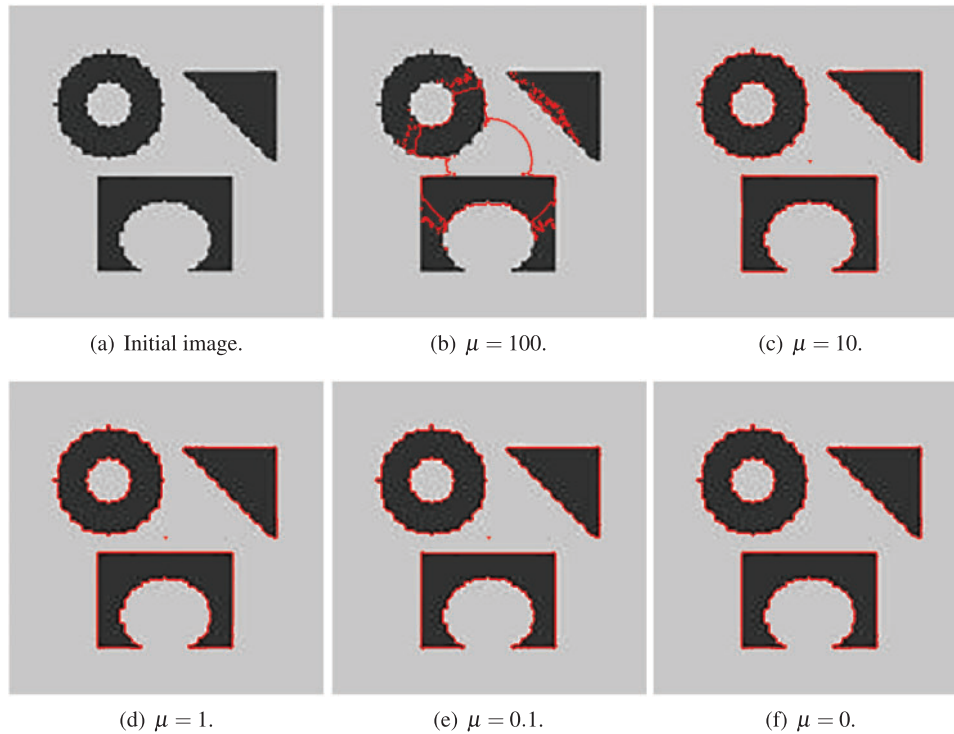


Figure 3: Evolution results for the initial image obtained using the GA-LRBF method combined with RK4 with different μ values

Table 2: Numerical results of using the GA-LRBF method combined RK4 with different μ values

μ	DICE	VOE	Iters	CPU (s)
100	49.7%	54.8%	2	3.1
10	99.5%	0.9%	2	3.2
1	99.9%	0.9%	2	3.4
0.1	99.6%	0.7%	2	3.2
0	99.6%	0.7%	2	2.9

Example 4.2. This experiment is designed to test the performance of the LRBF method. For this purpose, we apply the LRBF, GRBF and FDM schemes to discretize the spatial variables of the C-V model and the RK4 scheme for temporal discretization. Both circular and constant initial contours are considered.

Fig. 4 shows the results of the three numerical methods for a 238×200 pixel image with parameters of $\mu = 0$ and $\lambda_1 = \lambda_2 = 1$. For a constant initial contour $\phi_0 = a$ (a is a constant), since $\mu = 0$, we note that $a = 1$ should be avoided because it would cause the right-hand term in Eq. (10) to be 0, leading to stationary evolution. As shown in these figures, for a circular initial contour, the numerical results of all three methods converge to the image boundaries, whereas for a constant initial contour $\phi_0 = 2$, the FDM does not work, but the two RBF methods maintain good results. More results of these three methods are listed for comparison in Table 3. We conclude that the initial contour has a dramatic influence on the numerical results of the FDM but has little effect on the results of the two RBF methods. Thus, the RBF methods are effective computing tools for image segmentation; in particular, the LRBF method consumes less CPU time than the GRBF method. It is worth noting that the presented scheme is robust to and independent of the initialization, even without manual initialization; consequently, there is no need for complex and expensive reinitialization of the level set function to maintain numerical stability, which may be necessary in the traditional method [11].

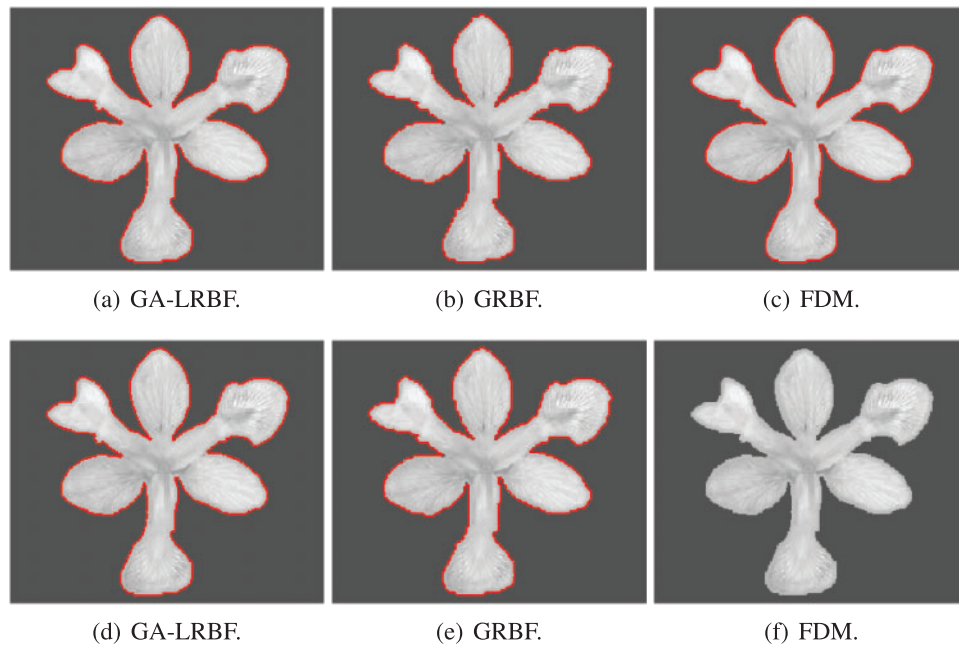


Figure 4: Evolution results of three numerical methods with (a–c) a circular initial contour and (d–f) a constant initial contour $\phi_0 = 2$

Table 3: Numerical results of these methods for two different initial contours

	LRBF		GRBF		FDM	
	Circle	Constant	Circle	Constant	Circle	Constant
DICE	97.8%	97.8%	96.8%	93.8%	97.8%	0.0%
VOE	0.0%	0.0%	4.7%	10.8%	0.1%	100.0%
Iters	2	4	2	3	120	120
CPU (s)	2.1	5.7	13.7	14.2	7.7	5.2

Example 4.3. *This experiment is designed to test the performance of RK4. We apply the GA-LRBF method to discretize the spatial variables of the C-V model, and the commonly used forward Euler scheme is introduced for numerical comparison. Two different initial contours (circular and constant) are used.*

We select three initial images as shown in Fig. 5. Table 4 lists numerical results of LRBF combined with RK4 and Forward Euler schemes for the edge segmentation problem. As expected, the convergence rate of the RK4 scheme is also much faster than that of the forward Euler scheme. Additionally, for clarity, Figs. 6 and 7 display the contour evolution on these three images. As we can see that, for the edge segmentation problem (Fig. 5a), the forward Euler method with a constant initial contour is less effective than this method with a circular initial contour. In particular, for images with holes (Figs. 5b and 5c), the forward Euler method cannot effectively separate the image from the background regardless of whether a constant or circular initial contour is used. However, RK4 is minimally affected by the above problems.

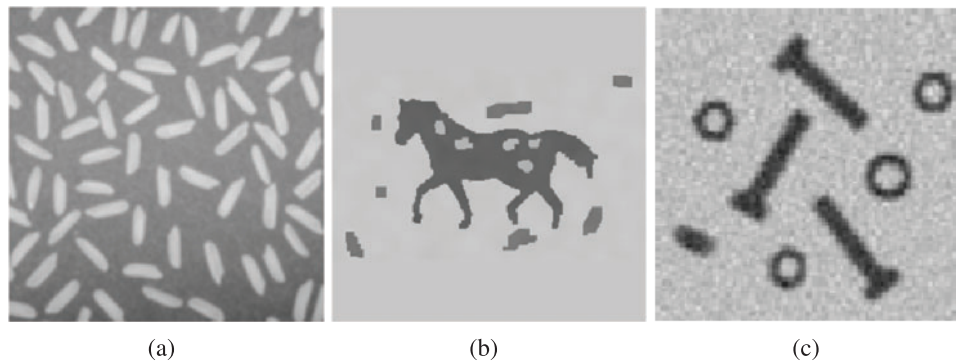


Figure 5: Three initial images, with pixel of (a) 256×256 , (b) 256×256 , and (c) 160×160

Table 4: Numerical results obtained by the RK4 scheme and the forward Euler scheme for temporal discretization

	LRBF-RK4				LRBF-forward Euler			
	Circle		Constant		Circle		Constant	
	Iters	CPU (s)	Iters	CPU (s)	Iters	CPU (s)	Iters	CPU (s)
Fig. 5a	2	2.8	2	3.8	2	2.2	11	6.1
Fig. 5b	2	2.7	5	6.2	2	2.3	11	5.9
Fig. 5c	3	2.0	5	2.5	2	1.3	11	2.9

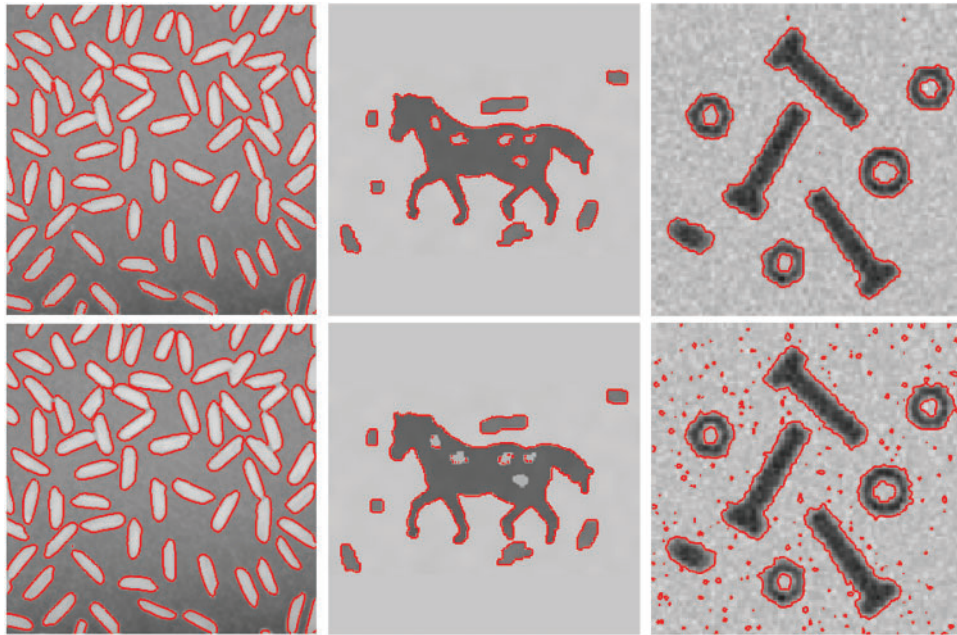


Figure 6: Evolution results obtained by RK4 (first row) and the forward Euler scheme (second row) with a circular initial contour

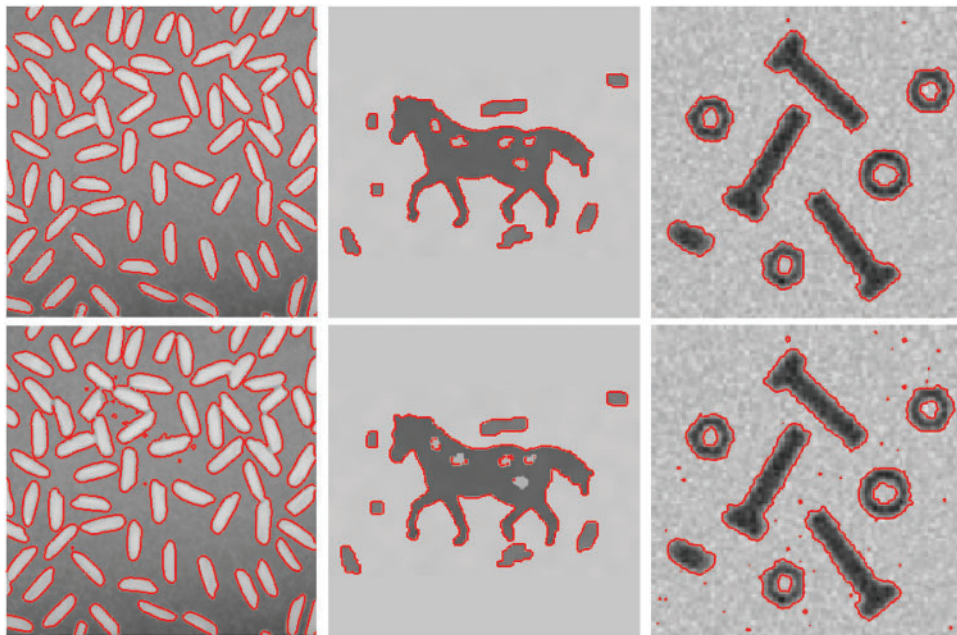


Figure 7: Evolution results obtained by RK4 (first row) and the forward Euler scheme (second row) with a constant initial contour $\phi_0 = 2$

5 Conclusion

In this paper, we presented a novel numerical method to solve the C-V model arising in image segmentation, in which the GA-LRBF and RK4 schemes were used for spatial and temporal variables, respectively. The LRBF method achieved improved efficiency and stability compared with the standard GRBF method because it used only a few neighboring points rather than all points in the domain. Furthermore, since the extensional function can be separated along each direction, it is suitable for the treatment of inhomogeneous image problems. Numerical results verify that the GA-LRBF method combined with RK4 can guarantee successful segmentation results with both circular and constant initial contours and even for images with holes. Therefore, this method is a powerful numerical tool for image segmentation. At present, the number of neighboring points is fixed for the GA-LRBF method; the question of how to determine the optimal number of points will be a focus of our work in the near future.

Acknowledgement: Authors would like to thank Dr. Rui Zhan at Guangdong University of Technology for providing many valuable suggestions for this research.

Funding Statement: This work was sponsored by Guangdong Basic and Applied Basic Research Foundation under Grant No. 2021A1515110680 and Guangzhou Basic and Applied Basic Research under Grant No. 202102020340.

Author Contributions: Shupeng Qiu: Conceptualization, Methodology, Software, Investigation, Formal Analysis, Writing Original Draft; Chujin Lin: Visualization, Investigation; Wei Zhao: Conceptualization, Funding Acquisition, Resources, Supervision, Writing Review & Editing.

Availability of Data and Materials: The authors confirm that the data supporting the findings of this study are available within the article.

Conflicts of Interest: The authors declare that they have no conflicts of interest to report regarding the present study.

References

1. Bennai, M. T., Guessoum, Z., Mazouzi, S., Cormier, S., Mezghiche, M. (2023). Multi-agent medical image segmentation: A survey. *Computer Methods and Programs in Biomedicine*, 232, 107444.
2. Foucart, A., Debeir, O., Decaestecker, C. (2023). Shortcomings and areas for improvement in digital pathology image segmentation challenges. *Computerized Medical Imaging and Graphics*, 103, 102155.
3. Mrinal, R. B. P. D., Javed, M. S. M. S. (2021). Autonomous driving architectures: Insights of machine learning and deep learning algorithms. *Machine Learning with Applications*, 6, 100164.
4. Long, J., Shelhamer, E., Darrell, T. (2015). Fully convolutional networks for semantic segmentation. *IEEE Transactions on Pattern Analysis and Machine Intelligence*, 39(4), 640–651.
5. Kass, M., Witkin, A., Terzopoulos, D. (1988). Snakes: Active contour models. *International Journal of Computer Vision*, 1(4), 321–331.
6. Osher, S., Sethian, J. A. (1988). Fronts propagating with curvature-dependent speed: Algorithms based on hamilton-jacobi formulations. *Journal of Computational Physics*, 79(1), 12–49.
7. Jeon, M., Alexander, M., Pedrycz, W., Pizzi, N. (2005). Unsupervised hierarchical image segmentation with level set and additive operator splitting. *Pattern Recognition Letters*, 26(10), 1461–1469.
8. Malladi, R., Sethian, J. A., Vemuri, B. C. (2009). Shape modeling with front propagation. *Journal of Architecture & Planning*, 74(74), 1935–1943.

9. Ngo, T. A., Zhi, L., Carneiro, G. (2017). Combining deep learning and level set for the automated segmentation of the left ventricle of the heart from cardiac cine magnetic resonance. *Medical Image Analysis*, 35, 159–171.
10. Mumford, D., Shah, J. (1989). Optimal approximations by piecewise smooth functions and associated variational problems. *Communications on Pure & Applied Mathematics*, 42(5), 577–685.
11. Chan, T. F., Vese, L. A. (2001). Active contours without edges. *IEEE Transactions on Image Processing*, 10(2), 266–277.
12. Xu, C., Li, C., Gui, C., Fox, M. D. (2005). Level set evolution without re-initialization. *2005 IEEE Computer Society Conference on Computer Vision and Pattern Recognition (CVPR'05)*, pp. 430–436. San Diego, CA, USA, IEEE Computer Society.
13. Wang, X. F., Huang, D. S., Xu, H. (2010). An efficient local chan-veese model for image segmentation. *Pattern Recognition*, 43(3), 603–618.
14. Li, Y., Kim, J. (2012). An unconditionally stable numerical method for bimodal image segmentation. *Applied Mathematics & Computation*, 219(6), 3083–3090.
15. Franke, C., Schaback, R. (1998). Solving partial differential equations by collocation using radial basis functions. *Applied Mathematics and Computation*, 93(1), 73–82.
16. Dehghan, M., Shokri, A. (2007). A numerical method for KdV equation using collocation and radial basis functions. *Nonlinear Dynamics*, 54(1), 136–146.
17. Majdisova, Z., Skala, V. (2018). Radial basis function approximations: Comparison and applications. *Applied Mathematical Modelling*, 51, 728–743.
18. Dereli, Y., Schaback, R. (2013). The meshless kernel-based method of lines for solving the equal width equation. *Applied Mathematics & Computation*, 219(10), 5224–5232.
19. Lenarduzzi, L., Schaback, R. (2017). Kernel-based adaptive approximation of functions with discontinuities. *Applied Mathematics & Computation*, 307, 113–123.
20. Rad, J. A., Hook, J., Larsson, E., von Sydow, L. (2017). Forward deterministic pricing of options using Gaussian radial basis functions. *Journal of Computational Science*, 24, 209–217.
21. Lotfi, Y., Parand, K. (2022). Efficient image denoising technique using the meshless method: Investigation of operator splitting RBF collocation method for two anisotropic diffusion-based PDEs. *Computers & Mathematics with Applications*, 113, 315–331.
22. Zhao, S., Oh, S. K., Kim, J. Y., Fu, Z., Pedrycz, W. (2022). Motion-blurred image restoration framework based on parameter estimation and fuzzy radial basis function neural networks. *Pattern Recognition*, 132, 108983.
23. Xie, X., Mirmehdi, M. (2011). Radial basis function based level set interpolation and evolution for deformable modelling. *Image and Vision Computing*, 29(2–3), 167–177.
24. Kashyap, K. L., Bajpai, M. K., Khanna, P. (2017). Globally supported radial basis function based collocation method for evolution of level set in mass segmentation using mammograms. *Computers in Biology and Medicine*, 87, 22–37.
25. Li, S., Li, X. (2016). Radial basis functions and level set method for image segmentation using partial differential equation. *Applied Mathematics and Computation*, 286, 29–40.
26. Gelas, A., Bernard, O., Friboulet, D., Prost, R. (2007). Compactly supported radial basis functions based collocation method for level-set evolution in image segmentation. *IEEE Transactions on Image Processing*, 16(7), 1873–1887.
27. Chen, C. S., Noorizadegan, A., Young, D. L., Chen, C. S. (2023). On the selection of a better radial basis function and its shape parameter in interpolation problems. *Applied Mathematics and Computation*, 442, 127713.

28. Ghalichi, S. S. S., Amirfakhrian, M., Allahviranloo, T. (2022). An algorithm for choosing a good shape parameter for radial basis functions method with a case study in image processing. *Results in Applied Mathematics*, 16, 100337.
29. Zhao, W., Hon, Y. C., Stoll, M. (2018). Localized radial basis functions-based pseudo-spectral method (LRBF-PSM) for nonlocal diffusion problems. *Computers & Mathematics with Applications*, 75(5), 1685–1704.
30. Zheng, Z., Li, X. (2022). Theoretical analysis of the generalized finite difference method. *Computers & Mathematics with Applications*, 120, 1–14.
31. Wang, F., Khan, M. N., Ahmad, I., Ahmad, H., Abu-Zinadah, H. et al. (2022). Numerical solution of traveling waves in chemical kinetics: Time-fractional fishers equations. *Fractals*, 30(2), 2240051.
32. Abbaszadeh, M., Dehghan, M. (2020). An upwind local radial basis functions-differential quadrature (RBFs-DQ) technique to simulate some models arising in water sciences. *Ocean Engineering*, 197, 106844.
33. Chang, H. H., Zhuang, A. H., Valentino, D. J., Chu, W. C. (2009). Performance measure characterization for evaluating neuroimage segmentation algorithms. *Neuroimage*, 47(1), 122–135.
34. Bo, L., Cheng, H. D., Huang, J., Tian, J., Tang, X. et al. (2010). Probability density difference-based active contour for ultrasound image segmentation. *Pattern Recognition*, 43(6), 2028–2042.

Appendix

Fig. 8 displays the segmentation results for a 256×256 pixel image obtained using the GRBF method combined with RK4 with $\mu = 100, 100, 10, 1, 0.1$ and 0 based on the C-V model. It can be observed that smaller parameter values lead to better results; in particular, when μ is zero, there is almost no influence on evolution. The results are listed for comparison in Table 5.

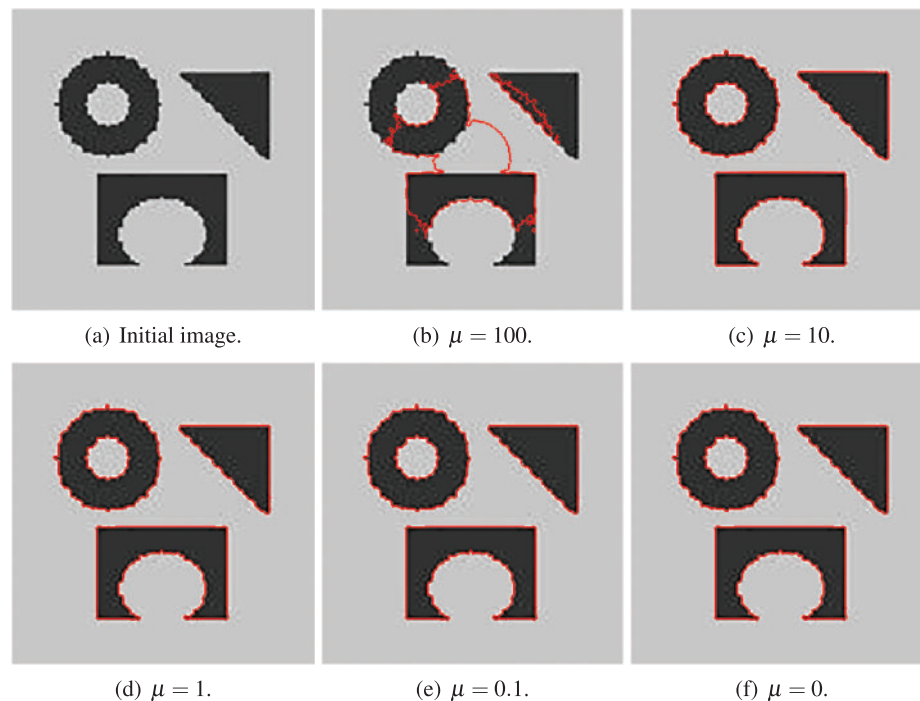


Figure 8: Evolution results for the initial image obtained using the GRBF method combined with RK4 with different μ values

Table 5: Numerical results of using the GRBF method combined with RK4 with different μ values

μ	DICE	VOE	Iters	CPU (s)
100	46.2%	82.1%	5	35.6
10	97.4%	5.2%	2	36.9
1	97.4%	5.2%	2	39.5
0.1	97.4%	5.2%	2	36.3
0	97.4%	5.2%	2	21.7